

Multi-code deep image prior based plug-and-play ADMM for image denoising and CT reconstruction

Chen Cheng^a, Qingping Zhou^{b,*}

^a*School of Mathematical Sciences, Shanghai Jiao Tong University, Shanghai, 200240, China*

^b*School of Mathematics and Statistics, HNP-LAMA, Central South University, Changsha, Hunan 410083, China*

Abstract

The use of the convolutional neural network based prior in imaging inverse problems has become increasingly popular. Current state-of-the-art methods, however, can easily result in severe overfitting, which makes a number of early stopping techniques necessary to eliminate the overfitting problem. To motivate our work, we review some existing approaches to image priors. We find that the deep image prior in combined with the handcrafted prior has an outstanding performance in terms of interpretability and representability. We propose a multi-code deep image prior, a multiple latent codes variant of the deep image prior, which can be utilized to eliminate overfitting and is also robust to the different numbers of the latent codes. Due to the non-differentiability of the handcrafted prior, we use the alternative direction method of multipliers (ADMM) algorithm. We compare the performance of the proposed method on an image denoising problem and a highly ill-posed CT reconstruction problem against the existing state-of-the-art methods, including PnP-DIP, DIP-VBTV and ADMM DIP-WTV methods. For the CelebA dataset denoising, we obtain 1.46 dB peak signal to noise ratio improvement against all compared methods. For the CT reconstruction, the corresponding average improvement of three test images is 4.3 dB over DIP, and 1.7 dB over ADMM DIP-WTV, and 1.2 dB over PnP-DIP along with a significant improvement in the structural similarity index.

Keywords: imaging inverse problems, overfitting, deep image prior, multi-code, CT reconstruction.

*Corresponding author

Email addresses: chengchen0301@sjtu.edu.cn (Chen Cheng), qpzhou@csu.edu.cn (Qingping Zhou)

1. Introduction

Deep learning-based approaches have currently achieved state-of-the-art quality for solving imaging inverse problems, including denoising [1, 2], computed tomography (CT) reconstruction [3–5] and many others. The observation is frequently contaminated with unknown noise, resulting in an ill-posed mathematical model of image reconstruction in solution space. In the case of CT restoration, it would be required to keep the number of detectors or angles as low as possible because excessive doses of applied radiation might be detrimental to patients. Furthermore, the observations are inevitably corrupted by noise. Indeed, there may be far fewer observations than unknowns, resulting in a strongly ill-posed issue in which multiple consistent images map to the same observations. As a result, one unsolved difficulty of image reconstruction approaches is selecting the optimal answer from a large number of possible solutions.

The choice of regularizer or prior plays a significant role in the solution of ill-posed inverse problems [6]. Deep neural network-based priors, such as generative adversarial networks (GAN) [7] and deep image priors (DIP) [8], have recently achieved high quality reconstruction for a variety of imaging problems. Methods based on GAN prior first train the GAN model $x = G_{\theta^*}(z)$ using ground truth images, where $G(\cdot)$ is GAN and θ^* denotes the internal parameters of the GAN after training, and z is a random variable in generative space. Once the training is finished, the reconstruction for a new measurement is given by solving a minimization problem [9]. However, training such a model usually requires a large dataset, limiting its utility in domains where data is scarce. DIP and its variants are another series of excellent approaches for solving image inverse problems which utilize deep neural networks without additional training data. It uses the inductive bias of an untrained convolutional neural network architecture as the prior, which eliminates the dependency on a large dataset. The reconstruction quality of DIP is comparable with some state-of-the-art data-driven methods [10, 11]. However, DIP approaches are often considerably overparamterized. As a result, the early stopping techniques are frequently critical and have attracted considerable research interest, and many methods have been developed to avoid overfitting, e.g., [12–15], just to name a few. [13, 15] add sparse additive noise to the optimization objective to avoid overfitting, and [12, 14] introduce a monitoring criterion during training procedures to prevent overfitting.

Many researchers seek to revolve this issue by combining DIP with other approaches to offer different perspectives and explanations for why their methods can mitigate overfitting [16–23]. In [17], an explicit regularizer named regularization by denoising (RED) is merged with DIP into an effective unsupervised recovery process.

In [18, 19], an averaging scheme of Bayesian perspective on DIP is used to reduce overfitting. [20] proposes a color image restoration method DIP-VBTV, which combines DIP with a vector bundle total variation (VBTV). Alternatively, [21] develops ADMM DIP-WTV for image restoration, which combines the DIP with weighted total variation (WTV). In [22], Stein’s unbiased risk estimator(SURE) is introduced as a surrogate to the generalization error. In [23], the number of trainable parameters is limited to reduce overfitting. In general, regularization terms such as L_1, L_2 are mostly applied to deep neural network weights. Because the network weights lack physical meaning, it is challenging to construct a good quality prior.

The method we propose is a variation of [11], which combines plug-and-play prior with DIP and solves the problem with the alternative direction method of multipliers method (ADMM). However, there is a significant difference: our method employs a multi-code prior based on DIP, which allows us to improve reconstruction quality by increasing the number of latent codes. Moreover, they exclusively use their method for natural imaging problems such as imaging inpainting, super-resolution, and denoising. Our method has been successfully applied to a highly ill-posed CT reconstruction problem. In the following, our proposal will be named MCDIP-ADMM, which uses ADMM to solve the minimization problem with a multi-code deep image prior.

Our contributions. Our proposed MCDIP-ADMM method is a simple yet effective algorithm that seeks to embrace the benefits of existing approaches while avoiding their drawbacks. The proposed method is

- (1) a general strategy to incorporate multiple features in latent space for DIP. It can also be naturally wrapped around other approaches, such as generative adversarial network (GAN) [7] and variational autoencoder (VAE) [24], just to name a few.
- (2) an effective and efficient method to prevent overfitting by incorporating MCDIP and ADMM method, presenting state-of-the-art results on a denoising problem and a severely ill-posed CT reconstruction problem.
- (3) a robust approach to the number of latent encoding codes, in which the MCDIP part of the hybrid prior can be learned from data.

The rest of the paper is organized as follows. Section 2 introduces the imaging inverse problem before reviewing and visualizing some of the most commonly used image priors for comparison. Section 3 introduces the DIP and multi-code generative prior, while Section 4 presents the proposed method. Section 5 presents numerical

experiments on image denoising and CT reconstruction problems, in which we investigate the previously discussed questions. Section 6 concludes with a discussion about future directions of this research.

2. Background and motivation

Image inverse problems. We start by presenting the formulation of the generic image inverse problem. Let X, Y be Hilbert or Banach spaces with inner product $\langle \cdot, \cdot \rangle$, data $\mathbf{y} \in Y \subset \mathbb{R}^m$ is related to $\mathbf{x} \in X \subset \mathbb{R}^n$ via the following imaging process:

$$\mathbf{y} = A\mathbf{x} \oplus \tau,$$

where A is the measurement operator that models the image acquisition process. It corresponds to an identity operator in the denoising problem and a sub-sampled radon transform in the CT reconstruction problem, to name a few. τ describes the noise in the measurement, with $\|\tau\| \leq \delta$. When Gaussian noise is assumed, the operator \oplus implies addition; when Poisson noise is assumed, it denotes a nonlinear operator. The aim is to obtain an approximation $\hat{\mathbf{x}}$ for the true solution \mathbf{x} .

Classical methods of solving this inverse problem involves a regularized optimization given by:

$$\hat{\mathbf{x}} = \arg \min_{\mathbf{x}} \mathcal{F}(A\mathbf{x}, \mathbf{y}) + \mathcal{R}(\mathbf{x}). \quad (1)$$

The term $\mathcal{F}(A\mathbf{x}, \mathbf{y})$ is fidelity loss that measures the consistency of the approximate solution to the observed data \mathbf{y} . Its specific formulation form depends on the noise statistics. For Gaussian noise, $\mathcal{F}(A\mathbf{x}, \mathbf{y}) = \frac{1}{2}\|A\mathbf{x} - \mathbf{y}\|_2^2$; and for Poisson noise, $\mathcal{F}(A\mathbf{x}, \mathbf{y}) = \langle \mathbf{1}, A\mathbf{x} \rangle - \langle \mathbf{y}, \log(A\mathbf{x}) \rangle$ with $\mathbf{1}$ being an all-ones vector. The second component $\mathcal{R}(\mathbf{x})$ is a regularization term that represents one’s prior knowledge of the unknown image. Regularizer selection is often one of the most critical steps in modeling and has attracted considerable attention in the literature.

Image prior. Handcrafted regularizers in the sense of optimization methods or priors in the sense of Bayesian inference, such as the most commonly used Gaussian prior, l^1 prior, and total variation (TV) prior, are traditionally easy to construct and often lead to explicit estimators [6]. Nevertheless, the fundamental limitation of these regularizers is that they may not be flexible or sophisticated enough to model image information. Deep learning-based regularizers, on the other hand, are generally much more effective and adaptable in extracting rich information. In this paper, we use the terms regularizer and prior interchangeably. We review the aforementioned classical priors into the application of image reconstruction methods and obtain intuitive

results. The density of Gaussian white noise with positivity constraint is

$$\pi_{\text{TG}}(\mathbf{x}) \propto \pi_+(\mathbf{x}) \exp\left(-\frac{1}{2\alpha^2}\|\mathbf{x}\|^2\right), \quad (2)$$

where $\pi_+(\mathbf{x}) = 1$ if $x_j > 0$ for all j and $\pi_+(\mathbf{x}) = 0$ otherwise. The $\|\cdot\|$ is the usual Euclidian norm. The ℓ^1 prior with positivity constraint is defined as

$$\pi_{\ell^1}(\mathbf{x}) = \alpha^n \pi_+(\mathbf{x}) \exp(-\alpha\|\mathbf{x}\|_1), \quad (3)$$

where $\|\mathbf{x}\|_1 = \sum_{i,j} |x_{ij}|$ and α is a hyperparameter. The total variation of the discrete image $\mathbf{x} = [x_1, x_2, \dots, x_n]^T$ is now defined as

$$\text{TV}(\mathbf{x}) = \sum_{j=1}^n V_j(\mathbf{x}), \quad V_j(\mathbf{x}) = \frac{1}{2} \sum_{i \in \mathcal{N}_j} \ell_{ij} |x_i - x_j|, \quad (4)$$

where \mathcal{N}_i is the index set of the neighbors of x_i and ℓ_{ij} is the length of the edge between the neighboring pixels. The discrete total variation density will now be given as

$$\pi_{\text{TV}}(\mathbf{x}) \propto \exp(-\alpha \text{TV}(\mathbf{x})), \quad (5)$$

where α is a positive constant.

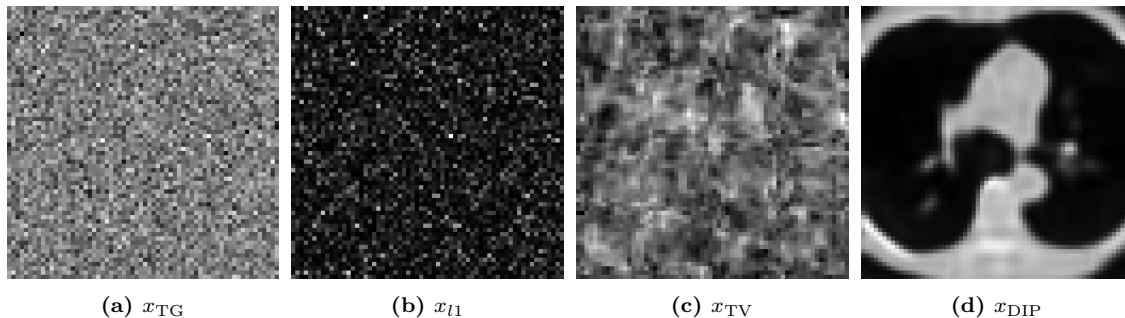


Fig. 1. One random sample from Gaussian white noise prior in Eq. (2), ℓ^1 prior in Eq. (3), total variation prior in Eq. (5) and deep image prior, respectively. From left to right, $x_{\text{TG}} \sim \pi_{\text{TG}}(\cdot)$, $x_{\ell^1} \sim \pi_{\ell^1}(\cdot)$, $x_{\text{TV}} \sim \pi_{\text{TV}}(\cdot)$, and x_{DIP} is the output of a randomly initialized DIP model with observed measurement as input.

In Fig. 1, we describe 64×64 noise images randomly drawn from distributions of the Gaussian prior, ℓ^1 prior, and the TV prior. The parameter α in the priors is chosen all equal to unity. For comparison, a sample from deep image prior (DIP) [8] is also displayed. As seen in Fig. 1, ℓ^1 prior can depict discontinuities, i.e., for some big leaps in the image. Besides sharp leaps, TV prior also exhibits clear correlation between nearby pixels. With its edge-preserving property, it has become the most

commonly used prior in image reconstruction field. A deep image prior sample, on the other hand, contains both the qualitative and quantitative features of the image, distinguishing it from other priors.

The implicit regularization prior of the deep image prior (DIP) [8] and the explicit one of regularization by denoising (RED) [17] are the two most commonly used priors in literature. RED employs regularization $\mathcal{R}(\mathbf{x}) = \frac{1}{2}\mathbf{x}^T(\mathbf{x} - f(\mathbf{x}))$ in which $f(\cdot)$ is a denoiser. DIP uses an untrained convolutional network $G(\mathbf{z}; \theta)$ as a surrogate of $\mathcal{R}(\mathbf{x})$, and optimizes over θ by $\theta^* = \arg \min_{\theta} \mathcal{F}(AG(\mathbf{z}; \theta), \mathbf{y})$ with \mathbf{z} randomly initialized and fixed, yielding reconstruction $\mathbf{x} = G(\mathbf{z}; \theta^*)$.

A current research trend is to combine explicitly handcrafted prior with deep learning-based prior for maximum benefits [11, 25, 26]. In this study, we analyze the DIP with multiple latent codes in combination with classical regularization methods like TV. With this approach, we expect to eliminate the necessity for early stopping in image denoising problems and typically highly ill-posed CT reconstruction problems.

3. Methodology

In this section, we first review the DIP method and associated techniques for dealing with the overfitting problem that has been identified while employing DIP. Then we introduce the structure of multi-code network and clarify its excellent expressiveness of images, which intrigues us to employ it for improved reconstruction quality.

3.1. Deep image Prior

The deep image prior (DIP) follows the generic template of the inverse problem (1) in Section 2. Instead of a regularization term $\mathcal{R}(\mathbf{x})$, the prior is replaced by the reparametrization $\mathbf{x} = G(\mathbf{z}; \theta)$, where G is a deep generative network with randomly initialized weights $\theta \in \Theta$ and a fixed input \mathbf{z} such as random white noise. The optimization formation can be written as follows:

$$\begin{aligned} \min_{\mathbf{x}, \theta} \quad & \mathcal{F}(A\mathbf{x}, \mathbf{y}) \\ \text{s.t.} \quad & \mathbf{x} = G(\mathbf{z}; \theta) \end{aligned} \tag{6}$$

The problem can then be solved by optimizing over the weights of the generator $G(\mathbf{z}; \theta)$ by a gradient descent method to minimize the data discrepancy of the network’s output.

The overfitting issue observed when using DIP suggests that the regularization term $\mathcal{R}(\mathbf{x})$ is required. On the other hand, DIP may incorporate state-of-the-art regularized methods as priors in more challenging inverse problems. Because these

regularizers are non-differentiable, they can not be solved using the vanilla gradient descent method in the form of an optimization problem; instead, the problem is reformulated by splitting the optimization variables into \mathbf{x} and \mathbf{w} :

$$\begin{aligned} \min_{\mathbf{w}, \mathbf{x}} \quad & \mathcal{F}(A\mathbf{w}, \mathbf{y}) + \mathcal{R}(\mathbf{x}) \\ \text{s.t.} \quad & \mathbf{x} = \mathbf{w} \end{aligned} \tag{7}$$

Since both two splitted variables are in two separated terms, the reformulated problem can be solved by altering direction method of multipliers(ADMM). Then by replacing the variable \mathbf{w} with a network $G(\mathbf{z}; \theta)$, the problem is reformulated in a hybrid version of DIP and plug-and-play priors [27]:

$$\begin{aligned} \min_{\theta, \mathbf{x}} \quad & \mathcal{F}(AG(\mathbf{z}; \theta), \mathbf{y}) + \mathcal{R}(\mathbf{x}) \\ \text{s.t.} \quad & \mathbf{x} = G(\mathbf{z}; \theta) \end{aligned}$$

The augmented Lagrangian of this new problem can be written as

$$\begin{aligned} \mathcal{L}_\rho(\mathbf{x}, \theta, \mathbf{u}) = & \mathcal{F}(AG(\mathbf{z}; \theta), \mathbf{y}) + \mathcal{R}(\mathbf{x}) \\ & + \frac{\rho}{2} \|\mathbf{x} - G(\mathbf{z}; \theta) + \mathbf{u}\|_2^2 - \frac{\rho}{2} \|\mathbf{u}\|_2^2, \end{aligned}$$

where \mathbf{u} is the dual variable and ρ is the penalty parameter. The corresponding ADMM steps for this augmented Lagrangian are

$$\begin{aligned} \mathbf{x}_{t+1} &= \text{prox}_{\frac{R}{\rho}}(G(\mathbf{z}; \theta_t) - \mathbf{u}_t) \\ \theta_{t+1} &= \underset{\theta}{\text{argmin}} \mathcal{L}_\rho(\mathbf{x}_{t+1}, \theta, \mathbf{u}_t) \\ \mathbf{u}_{t+1} &= \mathbf{u}_t + (\mathbf{x}_{t+1} - G(\mathbf{z}; \theta_{t+1})), \end{aligned}$$

which correspond to an \mathbf{x} -minimization step, a θ -minimization step and a dual ascent step respectively.

3.2. Multiple latent codes

Despite the success of DIP prior in image reconstruction, the expressiveness of the latent code is limited due to its finite dimensionality in the generated space. In other words, a single latent code \mathbf{z} might not be sufficient to express all the details of a certain image. A recent work [28] proposed to employ multiple latent codes $\{\mathbf{z}_n\}_{n=1}^N$, each of which can help reconstruct some sub-regions of the target image, and then compose their corresponding feature maps at some intermediate layer of the generator.

To be concrete, the generator $G(\cdot)$ is divided into two sub-networks $G_1^{(\ell)}(\cdot)$ and $G_2^{(\ell)}(\cdot)$. Here, ℓ is the index of the immediate layer to perform feature composition. For each \mathbf{z}_n , such a separation can extract the corresponding spatial feature $\mathbf{F}_n^{(\ell)} = G_1^{(\ell)}(\mathbf{z}_n)$ for further composition. Adaptive channel importance $\boldsymbol{\alpha}_n \in \mathbb{R}^C$ is introduced for each \mathbf{z}_n to help them align with different semantics. Here, C is the number of channels in the ℓ -th layer of $G(\cdot)$ and $\boldsymbol{\alpha}_n$ is a C -dimensional vector representing the importance of the corresponding channel of the feature map $\mathbf{F}_n^{(\ell)}$. With such composition, the image can be generated with

$$G(\mathbf{z}_1, \dots, \mathbf{z}_n; \theta) = G_2^{(\ell)} \left(\sum_{n=1}^N \mathbf{F}_n^{(\ell)} \odot \boldsymbol{\alpha}_n \right), \quad (8)$$

where \odot denotes the channel-wise multiplication as

$$\{\mathbf{F}_n^{(\ell)} \odot \boldsymbol{\alpha}_n\}_{i,j,c} = \{\mathbf{F}_n^{(\ell)}\}_{i,j,c} \times \{\boldsymbol{\alpha}_n\}_c. \quad (9)$$

Here, i and j indicate the spatial location, while c stands for the channel index.

4. Proposed method

We propose our multi-code deep image prior based on the DIP approach. Due to the limited representation ability of networks with a single latent code, we instead utilize a new network $G(\mathbf{z}_1, \dots, \mathbf{z}_n; \theta)$ with multiple inputs as the plug-and-play prior in Eq. (7), as illustrated in Fig. 2. It is the composition of a single generator $G(\cdot)$ with multiple latent codes $\{\mathbf{z}_n\}_{n=1}^N$. Then the optimization problem can therefore be written as follows:

$$\begin{aligned} \min_{\theta, \mathbf{x}} \quad & \mathcal{F}(AG(\mathbf{z}_1, \dots, \mathbf{z}_n; \theta), \mathbf{y}) + \mathcal{R}(\mathbf{x}) \\ \text{s.t.} \quad & \mathbf{x} = G(\mathbf{z}_1, \dots, \mathbf{z}_n; \theta) \end{aligned} \quad (10)$$

where the network $G(\mathbf{z}_1, \dots, \mathbf{z}_n, \theta)$ with multiple input features is defined as in Eq. (8), and $\mathcal{R}(\mathbf{x})$ is a l_∞ ball projection for natural image denoising problem (see details in Section 5.1.1). For CT image reconstruction problems, $\mathcal{R}(\mathbf{x}) = \lambda \text{TV}(\mathbf{x})$, where $\text{TV}(\cdot)$ is defined in Eq. (4). The regularization parameter λ determines the amount of the contribution of each term. If λ is large enough, the regularization term contributes more to the minimization issue than the data fidelity term. On the other hand, if λ is small enough, it frequently means that the regularizer is so weak that the data dominates the minimization issue. This circumstance is particularly undesirable in the ill-posed medical image reconstruction issue, as the problem is highly ill-posed

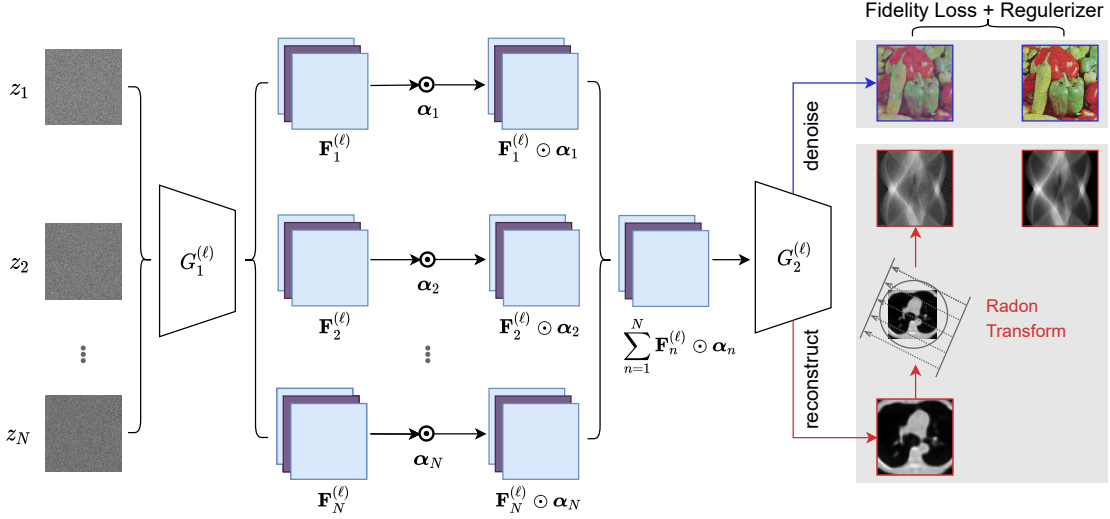


Fig. 2. Pipeline of the proposed Multi-Code Deep Image Prior (MCDIP-ADMM). The network $G(\cdot)$ of DIP is divided into two sub-networks $G_1^{(\ell)}(\cdot)$ and $G_2^{(\ell)}(\cdot)$. By employing multiple latent codes $\{\mathbf{z}_n\}_{n=1}^N$, we then obtain the restoration $\hat{\mathbf{x}} = G_2^{(\ell)}\left(\sum_{n=1}^N G_1^{(\ell)}(\mathbf{z}_n) \odot \alpha_n\right)$. The last two columns are comparison between the model results (left) and the true images (right) for denoising (blue arrow) and reconstruction (red arrow) respectively. The measurement operator A in Eq. (10) is an identity operator for denoising and a radon transform for CT image reconstruction.

and we require large contribution from the regularization term to produce accurate estimates of the unknown picture. In this regard, we should pick λ in such a manner that the impacts of the regularization term and the data term are properly balanced.

The new formation is also a updated version of DIP prior that the generator $G(\mathbf{z}; \theta)$ in DIP is substituted with the multi-code version of network $G(\mathbf{z}_1, \dots, \mathbf{z}_n; \theta)$. As a result, it retains the benefits of PnP-DIP in terms of limiting the overfitting issue observed when using DIP, and is hopeful of outperforming PnP-DIP thanks to the improved expressiveness of the network $G(\mathbf{z}_1, \dots, \mathbf{z}_n; \theta)$. To solve this new problem, we first write the augmented Lagrangian with scaled dual variable \mathbf{u} and penalty parameter ρ in the following form:

$$\begin{aligned} \mathcal{L}_\rho(\mathbf{x}, \theta, \mathbf{u}) = & \mathcal{F}(AG(\mathbf{z}_1, \dots, \mathbf{z}_n; \theta), \mathbf{y}) + \mathcal{R}(\mathbf{x}) \\ & + \frac{\rho}{2} \|\mathbf{x} - G(\mathbf{z}_1, \dots, \mathbf{z}_n; \theta) + \mathbf{u}\|_2^2 - \frac{\rho}{2} \|\mathbf{u}\|_2^2, \end{aligned}$$

Algorithm 1 MCDIP-ADMM

Input: Augmented Lagrangian \mathcal{L}_ρ , Regularizer R , Convolutional Neural Network G , Number of latent codes N , Number of iterations T , Step size for θ : β , Optimizer for θ : Opt

- 1: Sample N latent codes $\{\mathbf{z}_n\}_{n=1}^N$ from Gaussian distribution
- 2: Initialize $\theta_0, \mathbf{x}_0, \mathbf{u}_0$
- 3: **for** $t = 0, 1, \dots, T - 1$ **do**
- 4: $\mathbf{x}_{t+1} = \text{prox}_{\frac{R}{\rho}}(G(\mathbf{z}_1, \dots, \mathbf{z}_n; \theta_t) - \mathbf{u}_t) \leftarrow$ proximal step for \mathbf{x}
- 5: $g_\theta = \nabla_\theta \mathcal{L}_\rho(\mathbf{x}_{t+1}, \theta, \mathbf{u}_t) \leftarrow$ calculate gradient w.r.t. θ
- 6: $\theta_{t+1} = \theta_t - \beta \cdot \text{Opt}(\theta_t, g_\theta) \leftarrow$ update θ using gradient-based optimizer
- 7: $\mathbf{u}_{t+1} = \mathbf{u}_t + (\mathbf{x}_{t+1} - G(\mathbf{z}_1, \dots, \mathbf{z}_n; \theta_{t+1})) \leftarrow$ dual ascent step
- 8: **end for**

Output: reconstruction image \mathbf{x}_T

the optimization problem can be solved by the following ADMM steps:

$$\begin{aligned}\mathbf{x}_{t+1} &= \text{prox}_{\frac{R}{\rho}}(G(\mathbf{z}_1, \dots, \mathbf{z}_n; \theta_t) - \mathbf{u}_t) \\ \theta_{t+1} &= \underset{\theta}{\text{argmin}} \mathcal{L}_\rho(\mathbf{x}_{t+1}, \theta, \mathbf{u}_t) \\ \mathbf{u}_{t+1} &= \mathbf{u}_t + (\mathbf{x}_{t+1} - G(\mathbf{z}_1, \dots, \mathbf{z}_n; \theta_{t+1})).\end{aligned}$$

It should be noted that the θ -minimization step is often intractable. For computational efficiency, we take one gradient descent step for θ . This simple first-order update is sufficient to obtain good results in our experiments. Our method is summarized in Algorithm 1.

Relation to prior works. The main goal of the proposed MCDIP-ADMM approach is to boost the performance of the DIP framework by employing a multiple latent codes version of DIP, which is inspired by the multi-code GAN prior [28]. The weights of GAN are randomly initialized and kept fixed. In [28] the optimization problem is solved with respect to the multiple latent codes. In contrast, we optimize the weights of DIP while keeping the latent input codes fixed. Our proposed approach generalizes the PnP-DIP method proposed by Sun et al. [11]. PnP-DIP suggests a hybrid prior for Problem 6, which combines a handcrafted prior and DIP prior, to avoid the DIP’s overfitting phenomenon. However, it still has an overfitting issue when applied to denoising problems.

For image denoising and deblurring problems, DIP-VBTV [20] and ADMM DIP-WTV [21] have been recently proposed and achieved state-of-the-art performance.

Both methods propose a hybrid prior that combines DIP and a modified TV prior: a vector bundle total variation in DIP-VBTV and a weighted total variation in ADMM DIP-WTV. The main distinction is that our approach modifies the DIP term rather than the TV term of the hybrid prior. The numerical experiment on medical images presented by ADMM DIP-WTV is actually not a medical image reconstruction that restores the image from measurements, such as a sinogram for a CT problem, but rather an image denoising problem that restores the image from a corrupted image. With this insight, we incorporate a medical image reconstruction experiment to verify the performance of the proposed method and its comparisons.

5. Experiments and discussion

We apply the proposed method described in Section 4 to a denoising problem with the CelebA dataset [29], as well as a severely ill-posed inverse problem with the low-dose parallel beam (LoDoPaB) dataset [30]. To measure the quality of a reconstructed image, we compute the peak-signal-to-noise ratio (PSNR) and the structural similarity index measure (SSIM).

PSNR. PSNR represents the ratio of the maximum possible value to the reconstruction error, which is defined as a log-scaled version of the mean squared error (MSE) between the reconstruction $\hat{\mathbf{x}}$ and the ground truth image \mathbf{x} ,

$$\text{PSNR}(\hat{\mathbf{x}}, \mathbf{x}) = 10 \log_{10} \left(\frac{L^2}{\text{MSE}(\hat{\mathbf{x}}, \mathbf{x})} \right),$$

where the maximum image value $L = \max(\mathbf{x}) - \min(\mathbf{x})$, and $\text{MSE}(\hat{\mathbf{x}}, \mathbf{x}) = \frac{1}{n} \sum_{i=1}^n |\hat{x}_i - x_i|^2$. In general, a higher PSNR value indicates a better reconstruction quality.

SSIM. SSIM compares the overall structure of the image, including the luminance and contrast. It is based on assumptions about human visual perception. Results lie in the range $[0, 1]$, with higher values being better. The SSIM is calculated through a sliding window at M locations:

$$\text{SSIM}(\hat{\mathbf{x}}, \mathbf{x}) = \frac{1}{M} \sum_{j=1}^M \frac{(2\hat{\mu}_j\mu_j + C_1)(2\Sigma_j + C_2)}{(\hat{\mu}_j^2 + \mu_j^2 + C_1)(\hat{\sigma}_j^2 + \sigma_j^2 + C_2)}.$$

Here, $\hat{\mu}_j$ and μ_j are the average pixel intensities, $\hat{\sigma}_j$ and σ_j the variances and Σ_j the covariance of $\hat{\mathbf{x}}$ and \mathbf{x} at the j -th local window. Constants $C_1 = (K_1L)^2$ and $C_2 = (K_2L)^2$ stabilize the division. We use the same choices for the maximum image value L .

All experiments were carried out using Tesla V100S GPU with Pytorch [31]. Appropriate hyperparameters have been determined based on the performance on validation samples and are listed in Tables A1 and A2 in Appendix. We also provide the codes and the trained models in the Github repository when the manuscript has been accepted.

5.1. Implementation details

5.1.1. Denoising

The proposed method is illustrated with the CelebA dataset. All the image are resized into $128 \times 128 \times 3$ (49152 pixels). We add uniform noise $\epsilon \sim \mathcal{U}[-a, a]$ with $a = 50/255$. Due to the bounded noise, the proximal operator in \mathbf{x} -step of the proposed method corresponds to the projection to the l_∞ ball $\{\mathbf{x} \mid \|\mathbf{x} - \mathbf{b}\|_\infty \leq a\}$. We choose 10 images at random to tune the hyperparameters in the algorithm based on PSNR and SSIM.

We select 25 test images form the CelebA dataset. In our algorithm, we also apply the ADAM method [32] to optimize θ with learning rate 0.001, $\beta_1 = 0.9$, and $\beta_2 = 0.999$. The penalty parameter ρ is 1 in the augmented Lagrangian. For the convolutional neural network, we utilize a similar encoder-decoder architecture to that used in [11]. The parameters of the network are $n_u = n_d = [16, 32, 64, 128, 128]$, $n_s = [0, 0, 0, 0, 0]$, $k_d = k_u = 3$. See [8] for detailed explanation of these parameters. We also use a moving average to smooth the reconstructed images for better reconstruction as specified in [18].

We compare the proposed method to the state-of-the-art denoising methods PnP-DIP with l_∞ ball projection [11], DIP-VBTV [20] and ADMM DIP-WTV [21]. We also implement the original DIP [8] as baseline. For DIP and PnP-DIP, we employ the same network architecture and Adam optimizer [32] with the optimized learning rate as our proposed method. The penalty parameter $\rho = 1$ is used to implement the PnP-DIP and MCDIP-ADMM methods. The number of latent codes is 25, which is determined according to Fig. 7. For DIP-VBTV and ADMM DIP-WTV, we use the same network architecture and Adam optimizer with the optimized learning rate as in [20, 21]. Tables A1 and A2 in Appendix contain the hyperparameters of the models.

5.1.2. Computed tomography reconstruction

Since its introduction in the 1970s, X-ray computed tomography (CT) has become one of the most valuable diagnostic techniques in modern medical imaging. It provides images of the human body by assigning an X-ray attenuation coefficient to each pixel of the interested object. Most researchers are now focusing on minimizing

the quantity of potentially harmful radiation that a patient is exposed to throughout the scan process, which involves using fewer angles or lower intensity X-rays. However, both methods introduce special challenges in reconstruction, resulting in a significant drop in image quality.

Specifically, let x denote the unknown image to be reconstructed. We assume x is supported in the unit square Ω in \mathbb{R}^2 and we use a two-dimensional parallel beam CT. In this situation, the following Radon transform yields the projected data $f(s, \varphi)$ for each angle $\varphi \in [0, \pi]$ and distance from the origin $s \in \mathbb{R}$:

$$f(s, \varphi) = Ax(s, \varphi) = \int_{\mathbb{R}} x(L_{s,\varphi}(t)) dt,$$

where $L_{s,\varphi}(t)$ is the path of an X-ray beam by the distance from s and φ :

$$L_{s,\varphi}(t) = s\boldsymbol{\theta} + t\boldsymbol{\theta}^\perp, \quad \boldsymbol{\theta} = (\cos \varphi, \sin \varphi).$$

The goal of CT reconstruction problem is to recover the unknown image x from the sinogram of the transform for all pairs (s, φ) , also known as observations. Due to the reduced number of projection angle or the reduced size of detector, the inverse problem is ill-posed in the sense of Nashed [33]. A 256×256 ground truth image (Fig. 3, left) is chosen from the low-dose parallel beam (LoDoPaB) CT dataset [30]. The projection data, shown in Fig. 3 (right), is generated by plugging the true image into the Radon transform and then adding measurement noise to the result. The noise is Gaussian with a zero mean and a signal-to-noise ratio of 1%. For the simulation setup, 100 projections equispatically from 0 to π is used in the parallel Radon transform. Note that the regularizer λ has been manually tuned with the aim

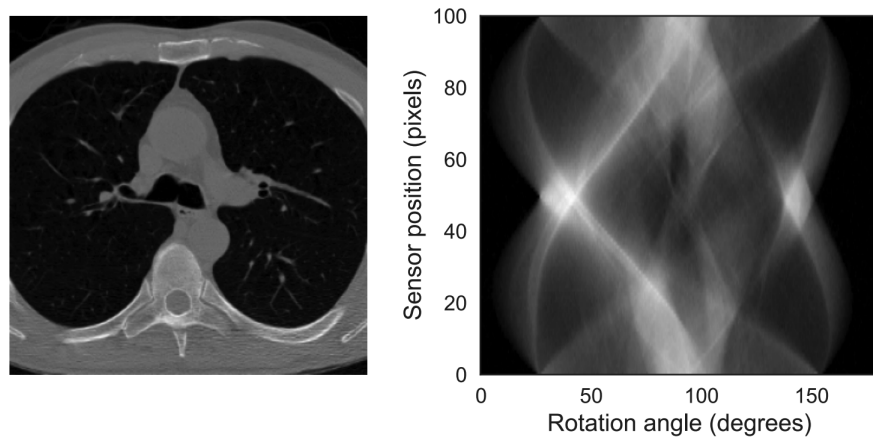


Fig. 3. Left: the ground truth image. Right: the projection data simulated from the ground truth.

of providing the best PSNR. Other settings are the same as in the denoising task.

5.2. Discussion on numerical results

5.2.1. Denoising

For the denoising problem, we employ the multi-code DIP method, which presents the best performance among four compared approaches: DIP, PnP-DIP, DIP-VBTV and ADMM DIP-WTV (see the results in Fig. 4). As expected, DIP exhibits a severe overfitting phenomenon, with PSNR and SSIM beginning to decline after about 300 iterations. DIP-VBTV suffers from the same problem though it has the highest peaks in both PSNR and SSIM. The MCDIP-ADMM approach has a little lower PSNR than PnP-DIP before 2000 iterations but a much higher PSNR than DIP-VBTV, PnP-DIP and DIP methods after 2000 iterations. After 10000 iterations, the proposed method beats ADMM DIP-WTV and outperforms the other four methods in PSNR. The SSIM of the proposed method is approximately equivalent to that of DIP and ADMM DIP-WTV, however, all these three are noticeably smaller than that of PnP-DIP before 100 iterations. Nonetheless, the SSIM of MCDIP-ADMM is remarkably higher than DIP, PnP-DIP and DIP-VBTV after 2000 iterations and again outperforms all comparisons after 10000 iterations. It is worth noting here that the standard deviation is rather small in the end of training (0.11 for MCDIP-ADMM and 0.12 for ADMM DIP-WTV), which shows the stability of the numerical scheme with the chosen parameters. The gap among four comparisons are quite minor after 10000 iterations. The final PSNR of PnP-DIP is only 0.15 dB larger than DIP and DIP-VBTV’s final PSNR is just 0.09 dB larger than DIP. Both suffer from overfitting as it first reaches the peak of PSNR and then gradually decreases. The final PSNR of ADMM DIP-WTV is 0.53 dB larger than DIP, which mitigate the

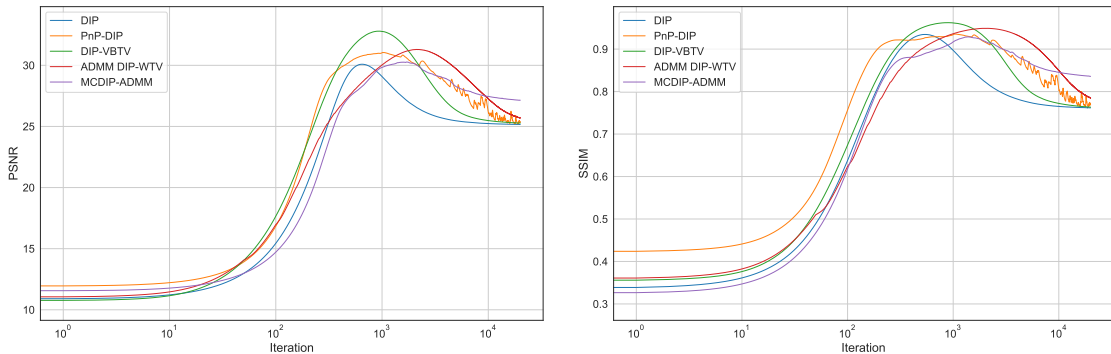


Fig. 4. Denoising: Evolution of the PSNR (left) and SSIM (right) with respect to the number of iterations for DIP, PnP-DIP, DIP-VBTV, ADMM DIP-WTV and MCDIP-ADMM. The solid line represents the average of these 25 images, and shade around the solid line depicts the one standard deviation.

overfitting issue to some extent. The MCDIP-ADMM method further improves the performance of ADMM DIP-WTV [21] with final PSNR 1.99 dB larger than DIP. Our proposed method escapes from the overfitting phenomenon since the PSNR nearly never decreases with training iterations. With the multi-code strategy combined with the deep image prior, the proposed method is able to mine richer prior information, improving performance.

Table 1: Average PSNR and SSIM and standard deviation over 25 test images.

	DIP	PnP-DIP	DIP-VBTV	ADMM DIP-WTV	MCDIP-ADMM
PSNR	25.16	25.31	25.27	25.69	27.15
	± 0.09	± 0.18	± 0.12	± 0.12	± 0.11
SSIM	0.76	0.77	0.76	0.78	0.83
	± 0.05	± 0.05	± 0.04	± 0.04	± 0.04

Table 1 illustrates the final average PSNR and SSIM, as well as their standard deviation over 25 test images, for DIP, PnP-DIP, DIP-VBTV, ADMM DIP-WTV and our MCDIP-ADMM methods. With PSNR 25.69 and SSIM 0.78, we find that ADMM DIP-WTV outperforms the other three comparisons. MCDIP-ADMM further outperforms ADMM DIP-WTV, with PSNR of 27.15 (+1.46) and SSIM of 0.83 (+0.05). It is worth mentioning that the main reason for this improvement is that the extracted features using multiple latent codes are more robust, which prevents the DIP-based model from overfitting. This improvement, however, comes at the expense of increased training time. Table 2 shows the computational time for aforementioned methods over 10000 iterations. It can be shown that MCDIP-ADMM is around 8.5 times more costly than DIP and 4.5 times more expensive than the other three techniques. Fig. 5 shows the PSNR and normalized loss with respect to CPU time, indicating that MCDIP-ADMM is the last among five methods to reach the peak of PSNR and converge in loss. The computation cost is worthwhile since our method is more stable with training iterations and escapes from the overfitting issue.

Table 2: Denoising: Computational time (in minutes) for different methods over 10000 iterations.

	DIP	PnP-DIP	DIP-VBTV	ADMM DIP-WTV	MCDIP-ADMM
time (in minutes)	2.54	4.14	4.30	4.89	21.8

We also test the results for higher resolution images with $512 \times 512 \times 3$. The evolution of the PSNR and SSIM values are similar to Fig. 4, thus we present the final and the best values in Table 3, and show the intermediate reconstructions at iterations

Table 3: Denoising: Final (best) PSNR and SSIM for five methods on higher resolution images.

	PSNR	SSIM
DIP	21.81(28.48)	0.46(0.86)
PnP-DIP	23.57(27.52)	0.57(0.85)
DIP-VBTV	27.54(29.93)	0.79(0.87)
ADMM DIP-WTV	28.13(29.07)	0.82(0.86)
MCDIP-ADMM	29.02(29.11)	0.84(0.84)

100, 1000 and 5000 in Fig. 6. The big gaps between the best and final value in first two columns indicate that DIP and PnP-DIP have been overfit on high-resolution images. In contrast, the gaps of DIP-VBTV, ADMM DIP-WTV and MCDIP-ADMM are much smaller in both PSNR and SSIM, with our method exhibiting the smallest gap: 0.09 in PSNR and 0 in SSIM. When multiple latent encoding features are incorporated into the prior, the overfitting phenomenon positively disappears.

A correlation exists between the number of encoding codes and the reconstruction quality. To gain a better understanding of their relationship, we test our method by varying the number of latent codes. We see in Fig. 7 that the more codes we apply, the better the reconstruction. However, this does not imply that the performance can be infinitely improved by increasing the number of codes. Fig. 7 shows that when the number of latent codes reaches 25, there is no significant improvement in terms of PSNR by involving more codes, and the fidelity loss continues to decrease until the number of latent codes approaches 35. Empirical strategies can be used to tune the number of latent codes. We analyze the observing metrics, such as PSNR or fidelity loss, with respect to the number of codes, which can then be determined till the measurement does not decrease. We believe that a number of codes ranging

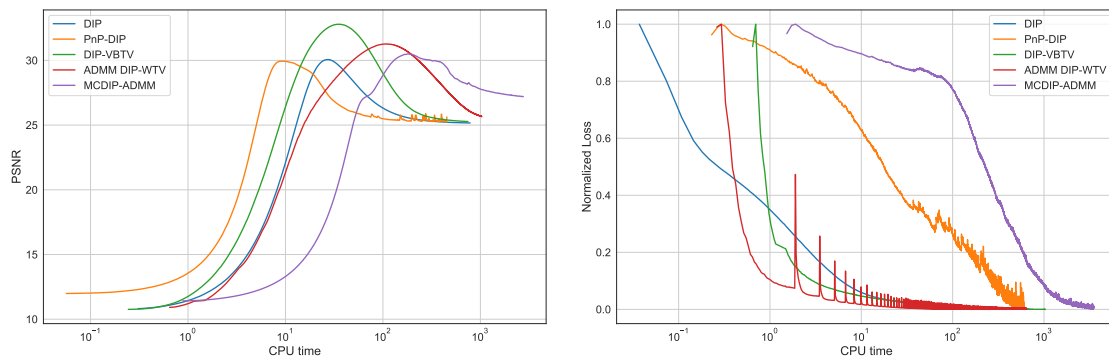


Fig. 5. Denoising: Evolution of the PSNR (left) and normalized loss (right) with respect to CPU time for DIP, PnP-DIP, DIP-VBTV, ADMM DIP-WTV and MCDIP-ADMM. Considering the difference of loss functions in various methods, the loss values are normalized from 0 to 1 for comparison.



Fig. 6. Denoising: Intermediate restorations of corrupted *pepper* image (top-right) provided by DIP-VBTV (first column), ADMM DIP-WTV (second column) and MCDIP-ADMM (third column) over ground truth (bottom right). From up to bottom: reconstructions at iterations 100, 1000 and 5000. The PSNR and SSIM values of different iteration numbers are displayed below the picture.

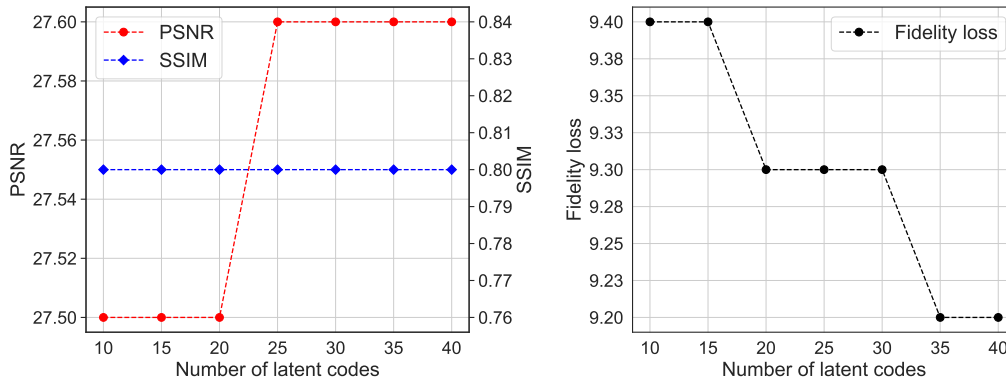


Fig. 7. Denoising: Plots of PSNR and SSIM values *versus* the number of codes (left) and mean fidelity loss *versus* the number of codes. The PSNR no longer increases when the number of latent codes reaches 25. The SSIM values are stable across different numbers of codes. For the number of latent codes greater than 35, the fidelity loss does not significantly decrease.

from 10 to 40 should be sufficient to an accurate and robust model.

5.2.2. Computed tomography reconstruction

Based on low-dose sparse-view X-ray data, we reconstruct a 256×256 lung image. Table 4 presents the PSNR, SSIM and fidelity loss of different methods. We compute the average PSNR improvement of three test images of the proposed method against its comparisons. The MCDIP-ADMM algorithm gives a 4.3 dB improvement over DIP, 1.7 dB over ADMM DIP-WTV, and 1.2 dB over PnP-DIP along with significantly higher SSIM values. It strongly shows that the MCDIP-ADMM model is superior than the other models in terms of PSNR and SSIM for all three test images. For image 2, the PSNR for the MCDIP-ADMM model is 32.45, compared to just 30.10 for PnP-DIP (the best one in comparisons) that reconstructs image without multiple latent codes. It is worth noting that the gap between the final PSNR and the best PSNR of MCDIP-ADMM, which is 3.06, is significantly lower than that of PnP-DIP, which is 4.93. For images 1 and 3, similar conclusions can be obtained. We can conclude that the proposed approach provides more accurate and robust restorations than its comparisons, largely thanks to its ability to extract multi-mode features from multiple latent codes. Fidelity loss $\mathcal{F}(A\mathbf{x}, \mathbf{y})$ in Eq. (1) measures the consistency between the forward projected reconstruction and the observations. It is commonly used to check for data discrepancies and it can provide additional insights into the performance of the reconstruction methods. For an ideal model, the fidelity loss $\mathcal{F}(A\hat{\mathbf{x}}, \mathbf{y})$ of the reconstruction $\hat{\mathbf{x}}$ would be close to the fidelity loss $\mathcal{F}(A\mathbf{x}, \mathbf{y})$ of the truth \mathbf{x} . For image 1, ADMM DIP-WTV performs best in terms of fidelity loss, with a fidelity loss of 158.09, which is extremely near to the fidelity loss of truth image. For image 2, the fidelity loss of ADMM DIP-WTV is slightly better than other approaches. For image 3, MCDIP-ADMM’s fidelity loss is the closest to the truth fidelity loss, whereas the other techniques’ fidelity losses are distant from truth fidelity loss.

Figs. 8, 10, and 12 provide a representative reconstruction for three test images using FBP, DIP, ADMM DIP-WTV, PnP-DIP and the proposed method. Our reconstruction is of the greatest quality, both visually and in terms of SSIM and PSNR. We find overall noise pollution in the images obtained using the FBP and the vanilla DIP approaches. Many artifacts can be seen in the DIP restoration as a result of severe overfitting. The fidelity loss of the ADMM DIP-WTV and MCDIP-ADMM is close to that of the ground truth, indicating that both methods mitigate overfitting. Other methods, including PnP-DIP, have terrible data consistency since their fidelity loss is significantly smaller than the ground truth. Furthermore, because the prior’s multi-encoding structure can collect more latent information of an image, this method is faster to achieve the maximum plateau region.

Table 4: Reconstruction: Final (best) PSNR, SSIM and fidelity loss for different methods on three test images. The greater PSNR or SSIM, the better the reconstruction quality. And the better the reconstruction model, the closer the fidelity loss is to that of the truth image. Best results are highlighted in bold. See Figs. 8, 10 and 12 for visualization.

	Image	Truth	FBP	CGNE	DIP	ADMM DIP-WTV	PnP-DIP	MCDIP-ADMM
PSNR	1		22.77	25.09	26.14 (29.66)	29.34 (29.34)	29.91 (30.06)	30.51 (30.51)
	2		20.2	22.56	27.97 (34.91)	30.06 (34.71)	30.1 (35.03)	32.45 (35.51)
	3		23.35	25.87	27.82 (30.57)	30.30 (30.30)	31.26 (31.42)	31.94 (31.94)
SSIM	1		0.55	0.66	0.74 (0.87)	0.87 (0.87)	0.87 (0.88)	0.89 (0.89)
	2		0.35	0.47	0.77 (0.96)	0.84 (0.96)	0.85 (0.96)	0.91 (0.96)
	3		0.57	0.69	0.82 (0.91)	0.91 (0.91)	0.91 (0.92)	0.93 (0.93)
Fidelity Loss	1	158.86	118.69	86.63	134.74 (134.74)	158.09 (158.09)	144.24 (144.16)	151.26 (151.26)
	2	203.25	148.54	112.46	181.02 (170.64)	183.54 (183.54)	174.33 (174.26)	179.10 (175.57)
	3	156.19	117.87	85.83	135.49 (135.49)	145.13 (145.13)	141.50 (141.50)	150.05 (150.05)

Figs. 9, 11 and 13 demonstrate the intermediate reconstructions of the ADMM DIP-WTV, PnP-DIP and MCDIP-ADMM methods at iterations 200, 20000 and 40000 on three test images. The first row shows that ADMM DIP-WTV and PnP-DIP tend to generate blurring and flat regions. Our proposed method, on the other hand, produces more realistic edges. We can see that the proposed method reconstructs most of the structures faster. Figs. 9, 11 and 13 show that the PSNR of the PnP-DIP increases and eventually decreases. For images 1 (Fig. 9) and 3 (Fig. 13), the PSNR of the ADMM DIP-WTV keeps increasing during training. For image 2 (Fig. 11), the PSNR of the ADMM DIP-WTV method decreases rapidly from 32.62 to 30.06. However, except in Fig. 11, the PSNR of MCDIP-ADMM grows continuously from iteration 200 to iteration 40000.

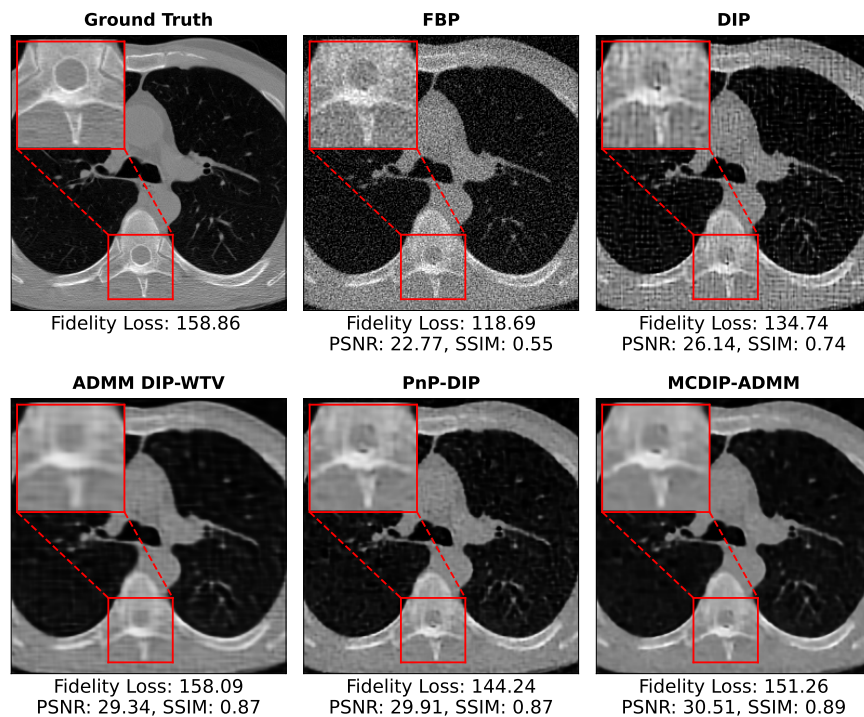


Fig. 8. Reconstruction of image 1: Comparison of reconstructions obtained using FBP, DIP, ADMM DIP-WTV, PnP-DIP and MCDIP-ADMM. The fidelity loss, PSNR and SSIM values are displayed below the picture, where fidelity loss measures the discrepancy between the observations and the noise-free projection of the reconstructed image.

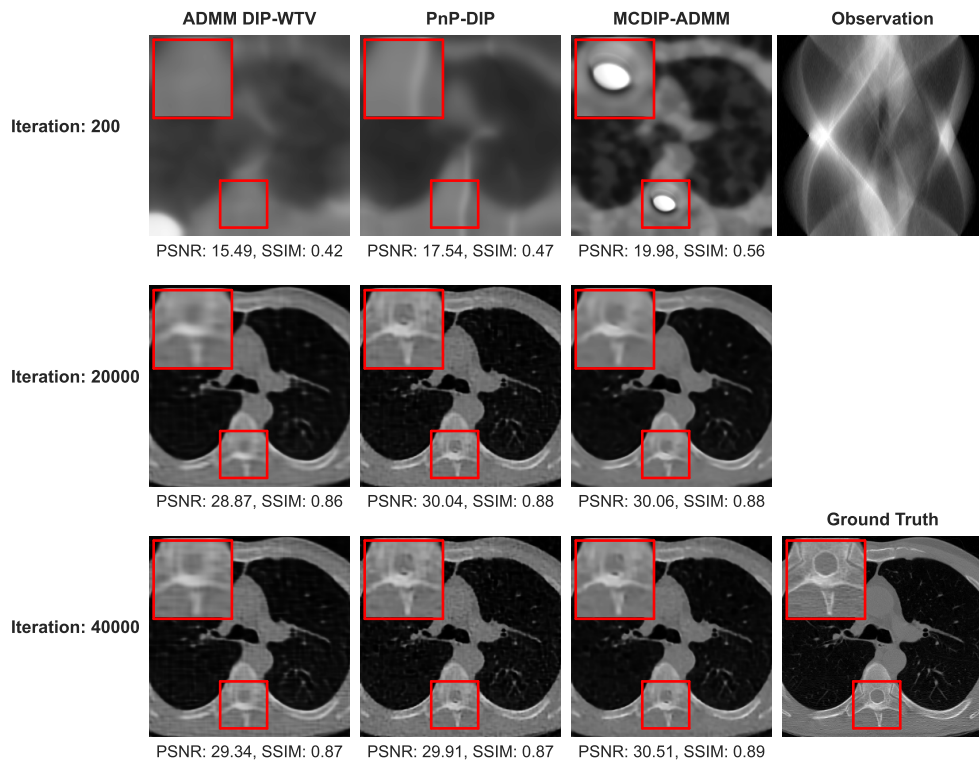


Fig. 9. Reconstruction of image 1: Intermediate restorations of corrupted sinogram (top-right) obtained by ADMM DIP-WTV (first column), PnP-DIP (second column) and MCDIP-ADMM (third column) over ground truth (bottom-right). From top to bottom: reconstructions at iterations 200, 20000 and 40000. The PSNR and SSIM values of different iterations are displayed below the picture.

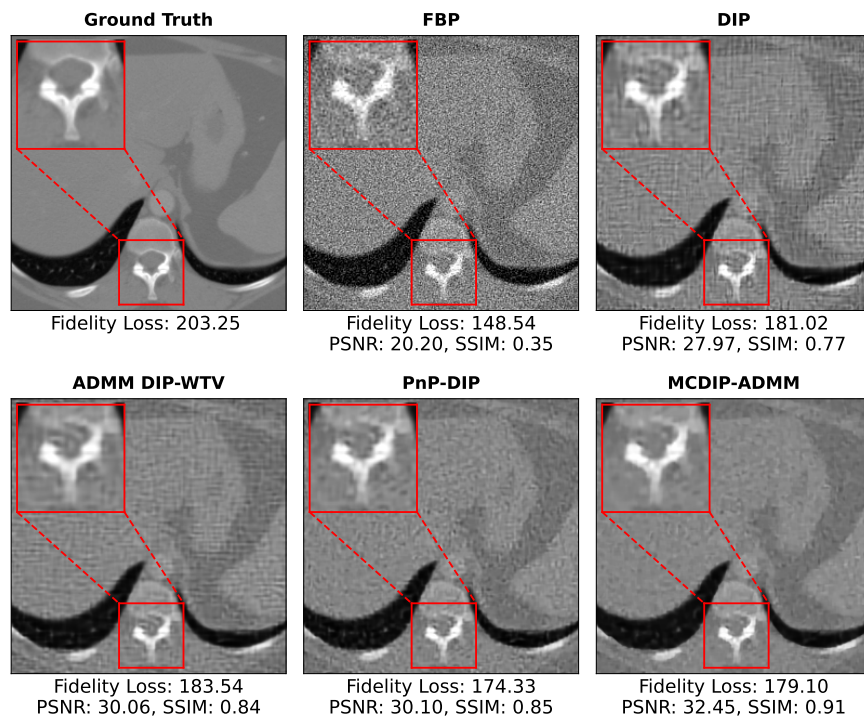


Fig. 10. Reconstruction of image 2: Comparison of reconstructions obtained using FBP, DIP, ADMM DIP-WTV, PnP-DIP and MCDIP-ADMM. The fidelity loss, PSNR and SSIM values are displayed below the picture, where fidelity loss measures the discrepancy between the observations and the noise-free projection of the reconstructed image.

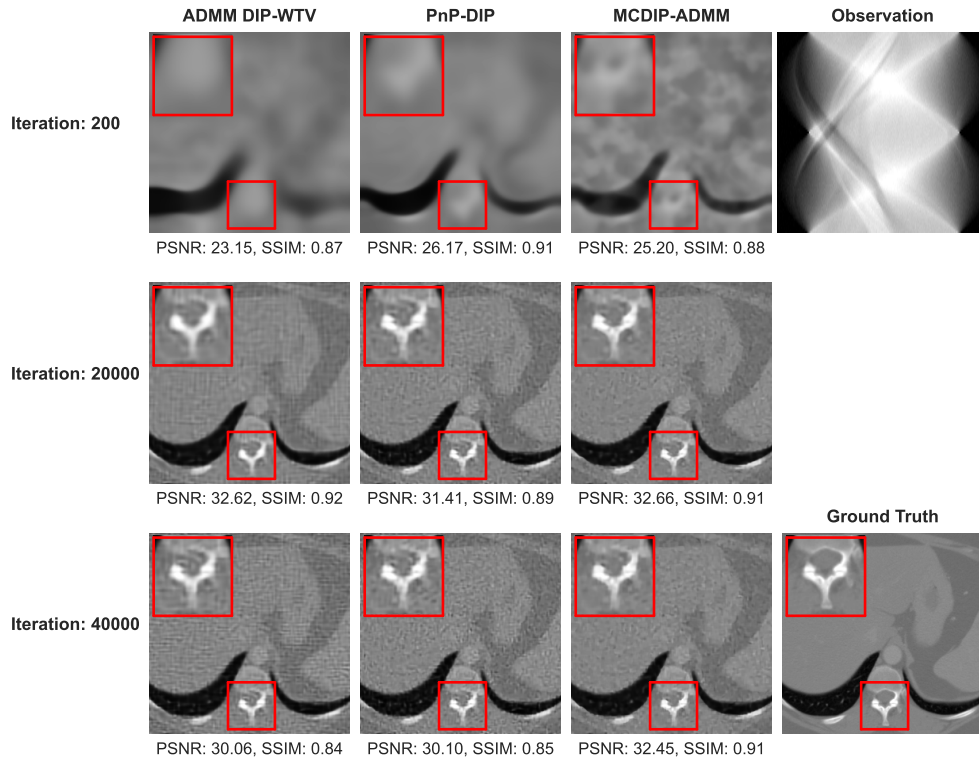


Fig. 11. Reconstruction of image 2: Intermediate restorations of corrupted sinogram (top-right) obtained by ADMM DIP-WTV (first column), PnP-DIP (second column) and MCDIP-ADMM (third column) over ground truth (bottom-right). From top to bottom: reconstructions at iterations 200, 20000 and 40000. The PSNR and SSIM values of different iterations are displayed below the picture.

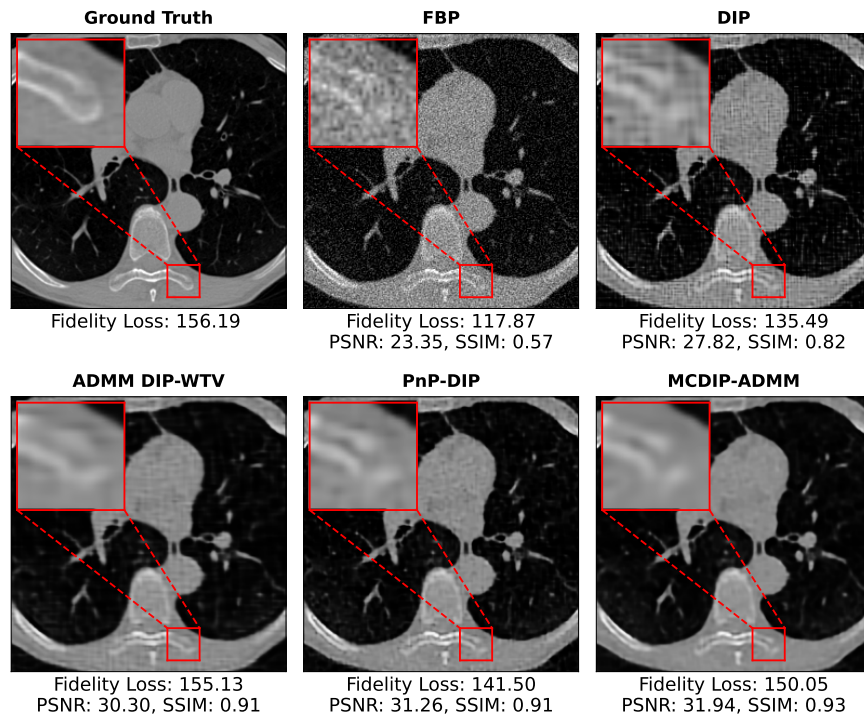


Fig. 12. Reconstruction of image 3: Comparison of reconstructions obtained using FBP, DIP, ADMM DIP-WTV, PnP-DIP and MCDIP-ADMM. The fidelity loss, PSNR and SSIM values are displayed below the picture, where fidelity loss measures the discrepancy between the observations and the noise-free projection of the reconstructed image.

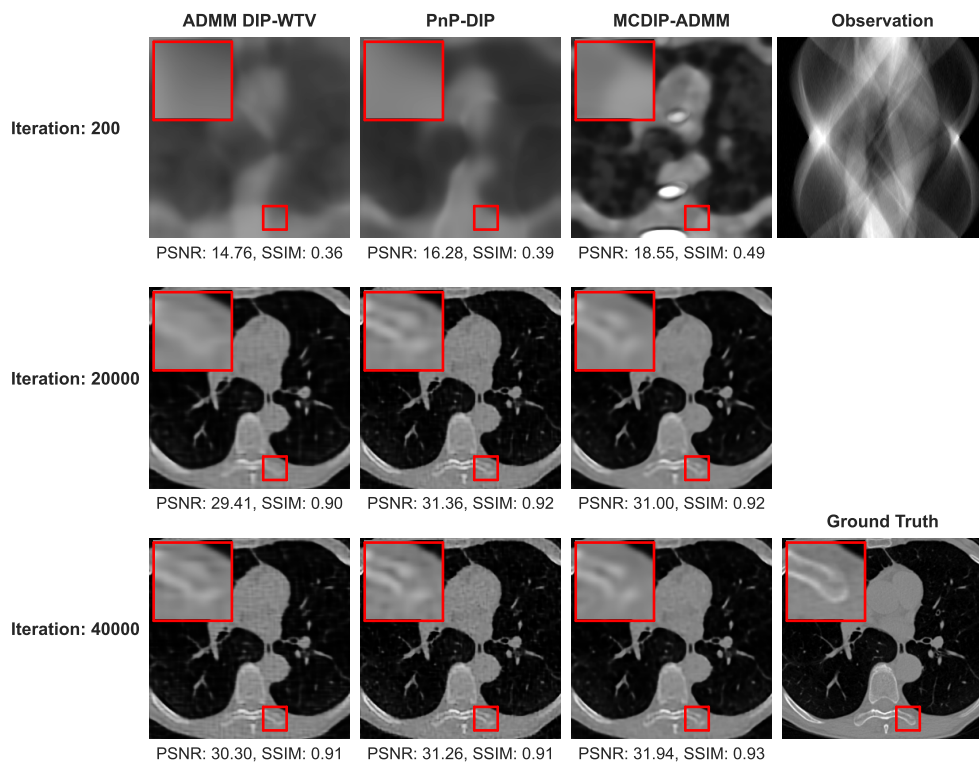


Fig. 13. Reconstruction of image 3: Intermediate restorations of corrupted sinogram (top-right) obtained by ADMM DIP-WTV (first column), PnP-DIP (second column) and MCDIP-ADMM (third column) over ground truth (bottom-right). From top to bottom: reconstructions at iterations 200, 20000 and 40000. The PSNR and SSIM values of different iterations are displayed below the picture.

6. Conclusion

This paper introduces a new approach (MCDIP-ADMM) for solving image inverse problems with a hybrid prior encoded by a deep convolutional network and total variation, with a focus on applications with single or limited training data. The approach is based on the deep image prior (DIP), which encodes image information using convolutional neural networks. It might be impossible to recover all the details of an image from a single latent code. As a result, we developed a multi-code DIP that employs multiple latent codes to reconstruct images. In addition, we enhance the multi-code DIP by combining it with the classical total variation (TV) regularization. Because the TV term is not differentiable, we utilize the alternating direction method of multipliers (ADMM) to solve the optimization problem with constraints. The performance of the method is demonstrated with an application to the CeleA dataset for image denoising, and it is discovered that the PSNR and SSIM values are robust to the number of latent codes and outperform competing state-of-the-art methods including the PnP-DIP [11], DIP-VBTV [20] and ADMM DIP-WTV [21] methods. We also present a low-dose sparse view computed tomography (CT) reconstruction problem to the LoDoPaB dataset. The MCDIP-ADMM method achieves the best data consistency without introducing artifacts in reconstruction results when compared to the other alternatives including the PnP-DIP and ADMM DIP-WTV methods. Furthermore, the proposed approach could be applied to other deep learning-based imaging inverse problems.

A main perspective for future work is to extend the proposed method to a Bayesian framework, for example, by developing a Bayesian approach [18, 34], and by replacing the standard DIP with a generative model where the prior has an explicit mathematical form, as in [35]. That work takes conditional normalizing flow to reconstruct the image, but it would be interesting to combine it with optimization algorithms.

Appendix

We present all the hyper-parameters in Tables A1 and A2.

Table A1: Hyperparameters of different models for natural image denoising and CT image reconstruction.

		Denoising	CT reconstruction
PnP-DIP	ρ	1	
MCDIP-ADMM	λ	0.01	4.0
MCDIP-ADMM	N	25	20
DIP-VBTV	λ	0.05	
	other	Color sapce: Eq.(2.24) in [20] h: diag(900,3000,3000) g: Eq.(2.9) in [20]	

Table A2: Hyperparameters of Adam optimizer for natural image denoising and CT image reconstruction. All experiments are performed by minimizing loss using the Adam optimizer in which the learning rate and β_1, β_2 are selected using a validation set.

	Denoising	CT reconstruction
lr	0.001	0.02
β_1	0.9	0.9
β_2	0.999	0.99

Table A3 shows PSNR and SSIM values of different methods with respect to iterations for *pepper* image denoising. Table A4 shows PSNR and SSIM values of different methods with respect to iterations for test image 1.

Table A3: Denoising: PSNR and SSIM values of different methods with respect to iterations.

Iterations	PSNR					SSIM				
	DIP	PnP-DIP	DIP-VBTV	ADMM DIP-WTV	MCIDP-ADMM	DIP	PnP-DIP	DIP-VBTV	ADMM DIP-WTV	MCIDP-ADMM
100	15.84	17.12	16.28	16.94	13.84	0.74	0.8	0.64	0.66	0.71
500	28.41	27.39	26.75	26.46	26.25	0.85	0.81	0.84	0.84	0.79
1000	26.13	26.93	29.47	28.66	27.4	0.7	0.78	0.87	0.86	0.79
2000	23.34	25.25	29.86	29.05	28.45	0.54	0.7	0.87	0.86	0.83
3500	22.24	23.75	28.76	28.64	28.86	0.48	0.59	0.84	0.84	0.84
5000	21.81	23.57	27.54	28.13	29.02	0.46	0.57	0.79	0.82	0.84

Table A4: CT reconstruction: PSNR and SSIM values of different methods with respect to iterations.

iterations	PSNR				SSIM			
	DIP	ADMM	PnP-DIP	MCIDP-ADMM	DIP	ADMM	PnP-DIP	MCIDP-ADMM
		DIP-WTV				DIP-WTV		
200	16.72	15.49	17.54	19.98	0.45	0.42	0.47	0.56
1000	22.71	18.85	24.77	26.37	0.66	0.55	0.75	0.8
5000	27.42	25.2	28.54	29.11	0.83	0.77	0.86	0.87
10000	29.15	27.31	29.65	29.57	0.86	0.83	0.88	0.87
15000	29.64	28.3	29.96	29.96	0.87	0.85	0.88	0.88
20000	29.17	28.87	30.04	30.06	0.85	0.86	0.88	0.88
30000	27.58	29.24	29.95	30.38	0.8	0.87	0.88	0.89
40000	26.14	29.34	29.91	30.51	0.74	0.87	0.87	0.89

Acknowledgements

The work is supported by the National Natural Science Foundation of China under Grant 12101614 and the Natural Science Foundation of Hunan Province, China, under Grant 2021JJ40715. We are grateful to the High Performance Computing Center of Central South University for assistance with the computations.

References

- [1] A. Houdard, C. Bouveyron, J. Delon, High-dimensional mixture models for unsupervised image denoising (HDMI), *SIAM Journal on Imaging Sciences* 11 (2018) 2815–2846.
- [2] A. Ashfahani, M. Pratama, E. Lughofer, Y.-S. Ong, DEV DAN: Deep evolving denoising autoencoder, *Neurocomputing* 390 (2020) 297–314.
- [3] D. O. Bagger, J. Leuschner, M. Schmidt, Computed tomography reconstruction using deep image prior and learned reconstruction methods, *Inverse Problems* 36 (2020) 094004.
- [4] D. Hu, Y. Zhang, J. Liu, S. Luo, Y. Chen, DIOR: Deep Iterative Optimization-based Residual-learning for Limited-angle CT Reconstruction, *IEEE Transactions on Medical Imaging* (2022).
- [5] A. Kofler, M. Haltmeier, C. Kolbitsch, M. Kachelrie, M. Dewey, A U-Nets cascade for sparse view computed tomography, in: *International Workshop on Machine Learning for Medical Image Reconstruction*, Springer, 2018, pp. 91–99.
- [6] J. Kaipio, E. Somersalo, *Statistical and computational inverse problems*, volume 160, Springer Science & Business Media, 2006.
- [7] I. Goodfellow, J. Pouget-Abadie, M. Mirza, B. Xu, D. Warde-Farley, S. Ozair, A. Courville, Y. Bengio, Generative adversarial nets, *Advances in neural information processing systems* 27 (2014).
- [8] D. Ulyanov, A. Vedaldi, V. Lempitsky, Deep image prior, in: *Proceedings of the IEEE conference on computer vision and pattern recognition*, 2018, pp. 9446–9454.
- [9] D. V. Patel, A. A. Oberai, GAN-Based Priors for Quantifying Uncertainty in Supervised Learning, *SIAM/ASA Journal on Uncertainty Quantification* 9 (2021) 1314–1343.

- [10] Z. Lai, K. Wei, Y. Fu, Deep Plug-and-Play Prior for Hyperspectral Image Restoration, *Neurocomputing* (2022).
- [11] Z. Sun, F. Latorre, T. Sanchez, V. Cevher, A Plug-and-Play Deep Image Prior, in: *ICASSP 2021-2021 IEEE International Conference on Acoustics, Speech and Signal Processing (ICASSP)*, IEEE, 2021, pp. 8103–8107.
- [12] Z. Shi, P. Mettes, S. Maji, C. G. Snoek, On measuring and controlling the spectral bias of the deep image prior, *arXiv preprint arXiv:2107.01125* (2021).
- [13] L. Ding, L. Jiang, Y. Chen, Q. Qu, Z. Zhu, Rank Overspecified Robust Matrix Recovery: Subgradient Method and Exact Recovery, *Advances in Neural Information Processing Systems* 34 (2021).
- [14] H. Wang, T. Li, Z. Zhuang, T. Chen, H. Liang, J. Sun, Early Stopping for Deep Image Prior, *arXiv preprint arXiv:2112.06074* (2021).
- [15] C. You, Z. Zhu, Q. Qu, Y. Ma, Robust recovery via implicit bias of discrepant learning rates for double over-parameterization, *Advances in Neural Information Processing Systems* 33 (2020) 17733–17744.
- [16] J. Liu, Y. Sun, X. Xu, U. S. Kamilov, Image restoration using total variation regularized deep image prior, in: *ICASSP 2019-2019 IEEE International Conference on Acoustics, Speech and Signal Processing (ICASSP)*, IEEE, 2019, pp. 7715–7719.
- [17] G. Mataev, P. Milanfar, M. Elad, DeepRED: Deep Image Prior Powered by RED, in: *Proceedings of the IEEE/CVF International Conference on Computer Vision Workshops*, 2019, pp. 0–0.
- [18] Z. Cheng, M. Gadelha, S. Maji, D. Sheldon, A Bayesian Perspective on the Deep Image Prior, in: *Proceedings of the IEEE/CVF Conference on Computer Vision and Pattern Recognition*, 2019, pp. 5443–5451.
- [19] D. Van Veen, A. Jalal, M. Soltanolkotabi, E. Price, S. Vishwanath, A. G. Dimakis, Compressed sensing with deep image prior and learned regularization, *arXiv preprint arXiv:1806.06438* (2018).
- [20] T. Batard, G. Haro, C. Ballester, Dip-vbvtv: A color image restoration model combining a deep image prior and a vector bundle total variation, *SIAM Journal on Imaging Sciences* 14 (2021) 1816–1847.

- [21] P. Cascarano, A. Sebastiani, M. C. Comes, G. Franchini, F. Porta, Combining weighted total variation and deep image prior for natural and medical image restoration via admm, in: 2021 21st International Conference on Computational Science and Its Applications (ICCSA), IEEE, 2021, pp. 39–46.
- [22] C. A. Metzler, A. Mousavi, R. Heckel, R. G. Baraniuk, Unsupervised learning with stein’s unbiased risk estimator, arXiv preprint arXiv:1805.10531 (2018).
- [23] R. Heckel, P. Hand, Deep decoder: Concise image representations from untrained non-convolutional networks, arXiv preprint arXiv:1810.03982 (2018).
- [24] D. P. Kingma, M. Welling, Auto-Encoding Variational Bayes, *stat* 1050 (2014) 1.
- [25] H. Wang, Q. Xie, Q. Zhao, D. Meng, A model-driven deep neural network for single image rain removal, in: Proceedings of the IEEE/CVF Conference on Computer Vision and Pattern Recognition, 2020, pp. 3103–3112.
- [26] Y. Fan, H. Wang, H. Gemmeke, T. Hopp, J. Hesser, Model-data-driven image reconstruction with neural networks for ultrasound computed tomography breast imaging, *Neurocomputing* 467 (2022) 10–21.
- [27] S. V. Venkatakrisnan, C. A. Bouman, B. Wohlberg, Plug-and-play priors for model based reconstruction, in: 2013 IEEE Global Conference on Signal and Information Processing, IEEE, 2013, pp. 945–948.
- [28] J. Gu, Y. Shen, B. Zhou, Image Processing Using Multi-Code GAN Prior, in: Proceedings of the IEEE/CVF conference on computer vision and pattern recognition, 2020, pp. 3012–3021.
- [29] Z. Liu, P. Luo, X. Wang, X. Tang, Deep learning face attributes in the wild, in: Proceedings of the IEEE international conference on computer vision, 2015, pp. 3730–3738.
- [30] J. Leuschner, M. Schmidt, D. O. Bager, P. Maass, LoDoPaB-CT, a benchmark dataset for low-dose computed tomography reconstruction, *Scientific Data* 8 (2021) 1–12.
- [31] A. Paszke, S. Gross, S. Chintala, G. Chanan, E. Yang, Z. DeVito, Z. Lin, A. Desmaison, L. Antiga, A. Lerer, Automatic differentiation in pytorch (2017).
- [32] D. P. Kingma, J. Ba, Adam: A method for stochastic optimization, arXiv preprint arXiv:1412.6980 (2014).

- [33] F. Natterer, The mathematics of computerized tomography, SIAM, 2001.
- [34] S. Kohl, B. Romera-Paredes, C. Meyer, J. De Fauw, J. R. Ledsam, K. Maier-Hein, S. Eslami, D. Jimenez Rezende, O. Ronneberger, A Probabilistic U-Net for Segmentation of Ambiguous Images, *Advances in neural information processing systems* 31 (2018).
- [35] A. Denker, M. Schmidt, J. Leuschner, P. Maass, J. Behrmann, Conditional normalizing flows for low-dose computed tomography image reconstruction, *arXiv preprint arXiv:2006.06270* (2020).